



Cite this: *Chem. Sci.*, 2022, 13, 4139

All publication charges for this article have been paid for by the Royal Society of Chemistry

# Bridging D–A type photosensitizers with the azo group to boost intersystem crossing for efficient photodynamic therapy†

Boyi Hao, Jiaxin Wang,  Chao Wang, Ke Xue, Minghui Xiao, Shuyi Lv and Chunlei Zhu \*

Photodynamic therapy (PDT) has attracted much attention in disease treatments. However, the exploration of a novel method for the construction of outstanding photosensitizers (PSs) with stimuli-responsiveness remains challenging. In this study, we, for the first time, report a novel and effective strategy to boost reactive oxygen species (ROS) generation by bridging donor–acceptor (D–A) type PSs with the azo group. In contrast to the counterpart without azo-bridging, the azo-bridged PSs exhibit remarkably enhanced ROS generation *via* both type-I and type-II photochemical reactions. Theoretical calculations suggest that azo-bridging leads to a prominent reduction in  $\Delta E_{ST}$ , thereby enabling enhanced ROS generation *via* efficient intersystem crossing (ISC). The resulting azo-bridged PS (denoted as Azo-TPA-Th(+)) exhibits a particularly strong bactericidal effect against clinically relevant drug-resistant bacteria, with the killing efficiency up to 99.999999% upon white light irradiation. Since azo-bridging generates an azobenzene structure, Azo-TPA-Th(+) can undergo *trans*-to-*cis* isomerization upon UV irradiation to form emissive aggregates by shutting down the ISC channel. By virtue of the fluorescence turn-on property of unbound Azo-TPA-Th(+), we propose a straightforward method to directly discern the effective photodynamic bactericidal dose without performing the tedious plate-counting assay. This study opens a brand-new avenue for the design of advanced PSs with both strong ROS generation and stimuli-responsiveness, holding great potential in high-quality PDT with rapid prediction of the therapeutic outcome.

Received 20th January 2022

Accepted 11th March 2022

DOI: 10.1039/d2sc00381c

rsc.li/chemical-science

## Introduction

Photodynamic therapy (PDT) has attracted much attention in disease treatments due to its prominent advantages, such as non-invasiveness, high spatiotemporal controllability, and low systemic toxicity.<sup>1,2</sup> In general, PDT primarily relies on three key components, that is, photosensitizers (PSs), a light source, and oxygen. In a typical process, PSs are excited to the excited singlet state ( $S_n$ ,  $n \geq 1$ ) by absorbing light energy, followed by intersystem crossing (ISC) to the excited triplet state ( $T_n$ ,  $n \geq 1$ ). The excitation energy is then consumed *via* an electron transfer process (type-I reaction<sup>3</sup>) and/or an energy transfer process (type-II reaction<sup>4</sup>) to the surrounding molecular oxygen ( $^3O_2$ ) to generate reactive oxygen species (ROS) (*e.g.*, superoxide radical anion ( $O_2^{\cdot-}$ ), hydroxyl radical ( $\cdot OH$ ), and singlet oxygen ( $^1O_2$ )), giving rise to the irreversible oxidation of bioactive molecules and thus bacterial/cell death.<sup>5</sup>

In view of the importance of PSs in PDT, a variety of PSs have been developed, such as porphyrins,<sup>6</sup> boron-dipyrromethene derivatives,<sup>7,8</sup> phthalocyanines,<sup>9</sup> and bacteriochlorins.<sup>10</sup> However, these traditional PSs are prone to aggregation when used in aqueous solutions due to the hydrophobic and rigid planar structures, leading to pronounced fluorescence quenching (known as aggregation-caused quenching (ACQ)) and reduced ROS generation.<sup>11</sup> In recent years, aggregation-induced emission (AIE) luminogens have emerged as an alternative class of PSs to overcome the ACQ problem.<sup>12–15</sup> Unlike traditional ACQ PSs, AIE PSs exhibit both strong fluorescence and efficient ROS generation in the aggregated state, which results from the remarkably suppressed nonradiative decay and thus favored ISC due to restricted intramolecular motions.<sup>16,17</sup> According to perturbation theory, the rate constant of ISC ( $k_{ISC}$ ) is described by the following equation:<sup>18,19</sup>

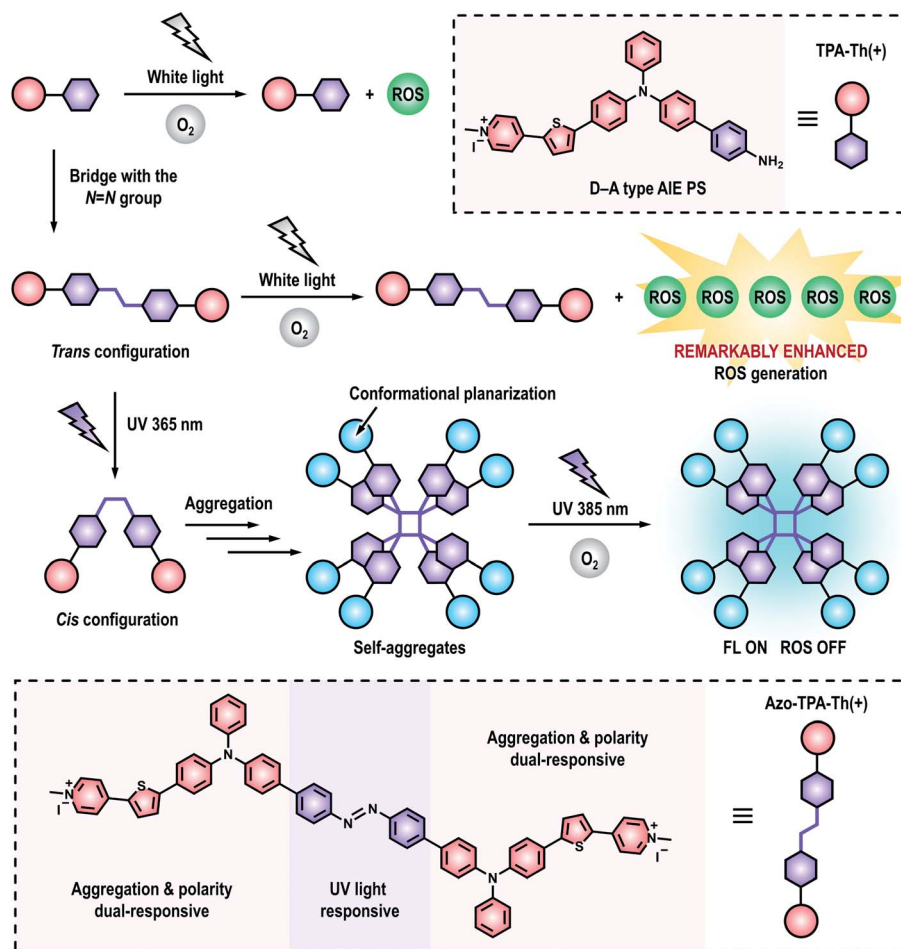
$$k_{ISC} \propto \xi_{ST}^2 / \exp(\Delta E_{ST}^2)$$

where  $\xi_{ST}$  and  $\Delta E_{ST}$  represent the spin–orbit coupling (SOC) constant and the energy gap between the singlet and triplet states, respectively. This equation suggests that the increase in  $\xi_{ST}$  and decrease in  $\Delta E_{ST}$  give rise to high  $k_{ISC}$  and thus efficient ISC. It is well acknowledged that the introduction of heavy

Key Laboratory of Functional Polymer Materials of Ministry of Education, State Key Laboratory of Medicinal Chemical Biology, Institute of Polymer Chemistry, College of Chemistry, Nankai University, Tianjin 300071, China. E-mail: chunlei.zhu@nankai.edu.cn

† Electronic supplementary information (ESI) available. See DOI: 10.1039/d2sc00381c





**Scheme 1** Schematic illustration showing the enhanced ROS generation by bridging D–A type PSs with the azo group as well as the responsiveness of the azo-bridged PSs to UV light.

atoms<sup>20–23</sup> (e.g., bromine, iodine, selenium, or platinum) favors the increase in  $\xi_{ST}$ . However, the presence of heavy atoms may cause potential toxicity when used in biological systems, limiting their biomedical applications. In this regard, tremendous efforts have been made to decrease  $\Delta E_{ST}$ .<sup>24</sup> To date, two general strategies have been established, that is, the construction of strong donor–acceptor (D–A) structures<sup>25–27</sup> and the fabrication of large conjugated systems *via* polymerization.<sup>28–30</sup> Despite the feasibility of these approaches in enhancing ROS generation, the resulting molecules either lack responsiveness to external stimuli or require complicated fabrication steps. In addition, polymeric PSs always suffer from batch-to-batch variability due to the compositional heterogeneity. As such, the continuous exploration of an effective strategy for enhanced photosensitization remains a research frontier.

Herein, we, for the first time, reported a novel and effective strategy to remarkably enhance photosensitization by covalently coupling D–A type PSs with the azo group for efficient PDT. First of all, we synthesized a D–A type AIE PS (denoted as TPA-Th(+)) as well as its azo-bridging counterpart (denoted as Azo-TPA-Th(+)). Surprisingly, the azo-bridged Azo-TPA-Th(+) exhibited remarkably enhanced ROS generation when compared to TPA-Th(+)

(Scheme 1). To authenticate the applicability of this approach, we also prepared another pair of D–A type AIE PSs (denoted as TPA(+) and Azo-TPA(+)) with shortened conjugation length. Even for the particularly weak PS (*i.e.*, TPA(+)), azo-bridging remained an effective strategy to enhance ROS generation. Theoretical calculations suggested that azo-bridging markedly decreased the  $\Delta E_{ST}$  of the resulting PSs, thereby facilitating ISC to boost the subsequent photosensitization process. Considering the prominent ROS generation capability of Azo-TPA-Th(+), we further evaluated its PDT effect against clinically relevant methicillin-resistant *Staphylococcus aureus* (MRSA). Under optimal conditions, the bacterial killing efficiency was determined to be 99.999999%. Due to the introduction of an azo-benzene structure<sup>31–33</sup> was formed in the resulting Azo-TPA-Th(+). Interestingly, UV irradiation initiated the photoisomerization of Azo-TPA-Th(+) from *trans* to *cis* configurations, leading to the formation of emissive aggregates due to the exposure of accessible hydrophobic domains. By virtue of the responsiveness of Azo-TPA-Th(+) to UV light, it was convenient to discern whether there existed excess, unbound Azo-TPA-Th(+) molecules *via* simple fluorescence tests, which actually reflected the binding threshold of Azo-TPA-Th(+) toward bacteria. In this case, the



effective PDT bactericidal dose could be forecasted within 1 h but without performing the tedious plate-counting assay that typically requires 24 h.

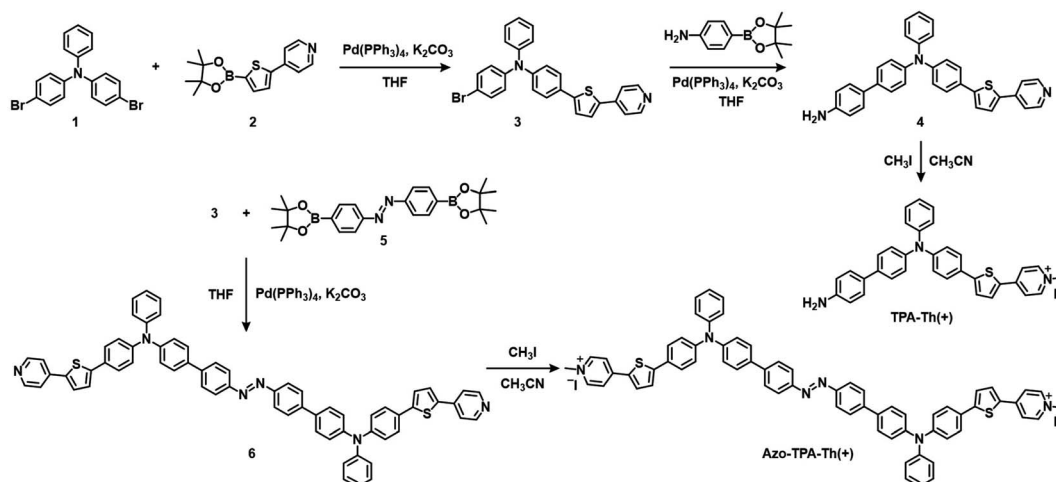
## Results and discussion

The synthetic routes to TPA-Th(+) and Azo-TPA-Th(+) are shown in Scheme 2. To construct D-A type AIE PSs, electron-donating and electron-withdrawing units as well as molecular rotators should be introduced into the molecular backbone. In terms of the synthesis of TPA-Th(+), compound **1** and compound **2** were reacted under Suzuki coupling conditions to give compound **3**. Next, aniline was attached to compound **3** through Suzuki coupling to yield compound **4**, which was followed by quaternization with iodomethane to obtain TPA-Th(+). For the synthesis of Azo-TPA-Th(+), two molecules of compound **3** were bridged by compound **5** through Suzuki coupling to give compound **6**, which was followed by quaternization with iodomethane to yield Azo-TPA-Th(+). The chemical structures of all compounds were verified by nuclear magnetic resonance spectrometry and high-resolution mass spectrometry (Fig. S1–S15†).

We first characterized the basic photophysical properties of TPA-Th(+) and Azo-TPA-Th(+). As shown in Fig. 1A, Azo-TPA-Th(+) and TPA-Th(+) exhibited a broad absorption in the range of 300–550 nm, with the absorption peaks located at *ca.* 465 nm. To study the AIE properties, a series of dimethyl sulfoxide (DMSO) solutions with different toluene fractions ( $f_t$ ) were prepared. As  $f_t$  increased, TPA-Th(+) and Azo-TPA-Th(+) started to form aggregates, resulting in enhanced emission in the range of 550–800 nm with the emission maxima located at *ca.* 600 and 630 nm, respectively (Fig. S31A–D†). Furthermore, the dynamic light scattering (DLS) data showed that the hydrodynamic diameters of TPA-Th(+) and Azo-TPA-Th(+) at  $f_t = 99\%$  were predominantly located at *ca.* 220 and 530 nm, respectively (Fig. S31E and F†). Taking the emission intensity at 600 and 630 nm as the variable parameters, respectively, the emission intensity ( $I$ ) of TPA-Th(+) and Azo-TPA-Th(+) in solutions with different  $f_t$  was compared with that in pure DMSO ( $I_0$ ) to plot the

AIE curves. As shown in Fig. 1B, when  $f_t$  was increased to 99%, the enhancement ratios for TPA-Th(+) and Azo-TPA-Th(+) were *ca.* 13- and 8-fold, respectively, suggesting the typical AIE feature. Notably, the smaller  $I/I_0$  for Azo-TPA-Th(+) was presumably attributed to the fast *trans*-to-*cis* isomerization of azobenzene that typically causes fluorescence quenching.<sup>34</sup> To confirm the photoisomerization of the azobenzene in Azo-TPA-Th(+), we performed a photoirradiation experiment to check the changes of its absorption spectra (Fig. S32†). However, both the  $\pi$ - $\pi^*$  and  $n$ - $\pi^*$  absorptions of azobenzene largely overlapped with the strong absorption of the TPA-Th(+) unit, making the spectral changes post  $\pi$ - $\pi^*$  and  $n$ - $\pi^*$  excitations hardly identifiable (Fig. S32A†). In this case, we enlarged the spectral regions that correspond to the  $\pi$ - $\pi^*$  and  $n$ - $\pi^*$  transitions of azobenzene. As shown in Fig. S32B and C,† after irradiation of Azo-TPA-Th(+) with 365 nm light, the intensities of the absorption peaks located between 310–350 nm and 450–490 nm exhibited opposite variation tendencies. Further irradiation with 450 nm light caused the absorption spectrum to basically return to its original state. Such a phenomenon was consistent with the *trans*-to-*cis* isomerization of azobenzene, suggesting the occurrence of photoisomerization.

We next assessed the ROS generation of TPA-Th(+) and Azo-TPA-Th(+) using three commercial indicators, 2',7'-dichlorofluorescein (DCFH),<sup>35</sup> 9,10-anthracenediyl-bis(methylene)-dimalonic acid (ABDA),<sup>36</sup> and dihydrorhodamine 123 (DHR-123)<sup>37</sup> (Fig. S33–S36†). DCFH is a non-fluorescent probe that responds to all kinds of ROS by converting to highly fluorescent 2',7'-dichlorofluorescein (DCF). Taking the emission intensity at 525 nm as the variable parameter, we recorded the relative emission intensity ( $I/I_0$ ) of DCFH in the presence of TPA-Th(+) and Azo-TPA-Th(+) upon white light irradiation. As shown in Fig. 1C, as the irradiation time prolonged, the emission signals for both groups gradually increased and reached a plateau after 40 s. It should be pointed out that the enhancement ratio for the Azo-TPA-Th(+) group was *ca.* 40-fold, which was much higher than that for the TPA-Th(+) group (*ca.* 20-fold) as well as that for the group with two equivalents of TPA-Th(+) (2 eq. TPA-Th(+), *ca.*



Scheme 2 Synthetic routes to TPA-Th(+) and Azo-TPA-Th(+).



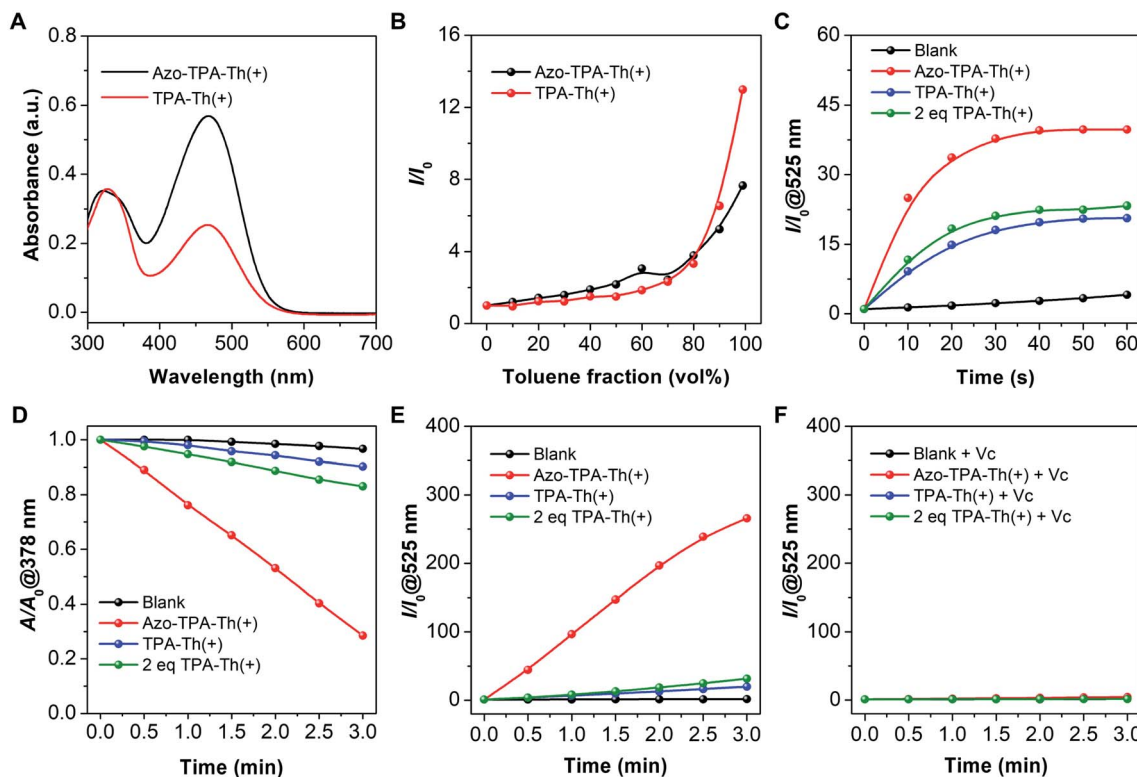


**Fig. 1** Photophysical and photochemical characterizations of TPA-Th(+) and Azo-TPA-Th(+). (A) UV-vis spectra of Azo-TPA-Th(+) and TPA-Th(+) in DMSO (20 μM). (B) Plots of the relative emission intensity ( $I/I_0$ ) of Azo-TPA-Th(+) at 630 nm and TPA-Th(+) at 600 nm as a function of toluene fractions ( $f_t$ ) in DMSO/toluene mixtures (20 μM,  $\lambda_{ex} = 488$  nm). (C) Plots of the relative emission intensity ( $I/I_0$ ) at 525 nm of DCFH in the presence of Azo-TPA-Th(+) and TPA-Th(+) upon white light irradiation.  $A_0$  and  $A$  represent the absorbance at 378 nm before and after white light irradiation, respectively. (E) Plots of the relative emission intensity ( $I/I_0$ ) at 525 nm of DHR-123 in the presence of Azo-TPA-Th(+) and TPA-Th(+) as a function of irradiation time. (F) Plots of the relative emission intensity ( $I/I_0$ ) at 525 nm of DHR-123 in the presence of Azo-TPA-Th(+) and TPA-Th(+) supplemented with Vc as a function of irradiation time.

23-fold), suggesting the remarkably enhanced photosensitization post azo-bridging. To further specify the type of generated ROS, ABDA and DHR-123 were utilized to reflect the production of type-II and type-I ROS, respectively. In the presence of  $^1O_2$ , ABDA is transformed into its endoperoxide form, leading to a decrease in absorbance. In this case, the proportion of the absorbance at 378 nm after and before irradiation ( $A/A_0$ ) is inversely correlated with the amount of  $^1O_2$ . As shown in Fig. 1D, the Azo-TPA-Th(+) group exhibited the lowest  $A/A_0$  value (0.28), which was much lower than that of the TPA-Th(+) group (0.9) as well as that of the 2 eq. TPA-Th(+) group (0.8). In the presence of type-I ROS, DHR-123 is oxidized to the fluorescent rhodamine 123. Taking the emission intensity at 525 nm as the variable parameter, we recorded the relative emission intensity ( $I/I_0$ ) of DHR-123 in the presence of Azo-TPA-Th(+) and TPA-Th(+) upon white light irradiation. Surprisingly, the enhancement ratio of the Azo-TPA-Th(+) group was up to 265-fold, which was astonishingly higher than those of the TPA-Th(+) (20-fold) and 2 eq. TPA-Th(+) (31-fold) groups (Fig. 1E). Besides, the addition of vitamin C (Vc) completely inhibited the conversion of DHR-123 into its fluorescent form due to the efficient consumption of type-I ROS via a redox reaction (Fig. 1F). To further confirm the generation of  $O_2^{\cdot-}$  by the sensitization of

Azo-TPA-Th(+), we also performed electron spin resonance (ESR) experiments with 5,5-dimethyl-1-pyrroline *N*-oxide (DMPO) as the spin trapping agent. As shown in Fig. S37,† in the presence of DMPO and Azo-TPA-Th(+), there was a characteristic ESR signal for the DMPO/ $O_2^{\cdot-}$  adduct under white light irradiation, suggesting the generation of  $O_2^{\cdot-}$ . These results altogether demonstrated that bridging D-A type PSs with the azo group was an effective strategy to boost the generation of both type-II and type-I ROS.

To confirm the applicability of azo-bridging enhanced photosensitization, another pair of D-A type PSs with shortened conjugation length (denoted as TPA(+) and Azo-TPA(+)) were prepared using the synthetic routes similar to TPA-Th(+) and Azo-TPA-Th(+) (Scheme S1 and Fig. S16–S30†). As anticipated, the absorption maxima of TPA-Th(+) and Azo-TPA-Th(+) were blue-shifted to *ca.* 430 nm as a result of the decreased  $\pi$  conjugation (Fig. S38A†). Similarly, TPA-Th(+) exhibited a typical AIE phenomenon, with the enhancement ratio of *ca.* 16 (Fig. S38B and S39A and C†). However, only 1-fold enhancement was observed for Azo-TPA(+) (Fig. S38B and S39B and D†), which likewise resulted from the quenching effect of azobenzene. The DLS data also suggested the formation of large aggregates at  $f_t = 99\%$  for TPA(+) and Azo-TPA(+), respectively (Fig. S39E and F†).





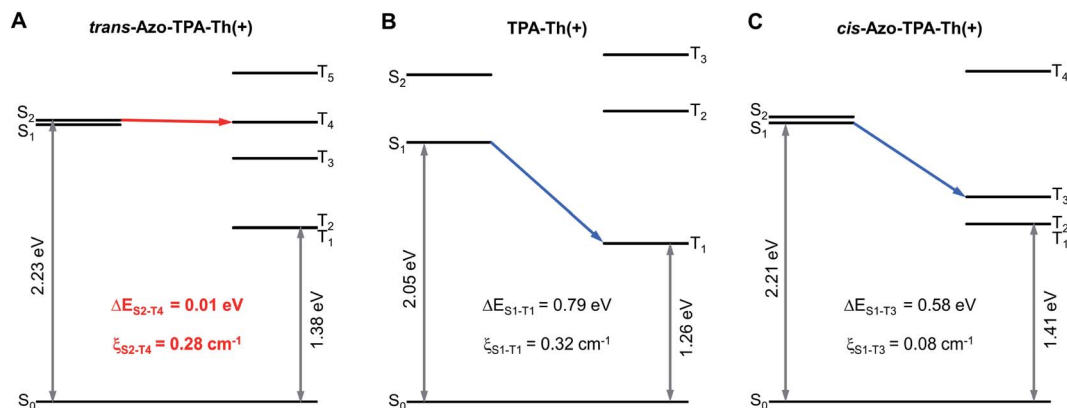


Fig. 2 Energy level diagrams and calculated  $\xi_{ST}$  between different singlet–triplet channels for (A) *trans*-Azo-TPA-Th(+), (B) TPA-Th(+), and (C) *cis*-Azo-TPA-Th(+).

In addition, ROS measurements demonstrated that Azo-TPA(+) showed the strongest capability in the generation of total, type-II, and type-I ROS (particularly type-I ROS) when compared to TPA(+) and two equivalents of TPA(+) (2 eq. TPA(+)) (Fig. S38C–F and S40–S42†). Due to the weakened D–A effect, TPA(+) and Azo-TPA(+) showed decreased ROS generation relative to TPA-Th(+) and Azo-TPA-Th(+), respectively. However, azo-bridging transformed a remarkably weak PS (*i.e.*, TPA(+)) into a moderately strong PS (*i.e.*, Azo-TPA(+)), which once again evidenced the effectiveness of this strategy in boosting ROS generation. It should be noted that azo-bridging did not contribute to the extension of effective conjugation, which could be clearly indicated when comparing the absorption spectra of the azo-bridged and non-bridged PSs. As shown in Fig. 1A and S38A,† the absorption maxima in the visible region of all azo-bridged PSs were basically identical to those of the corresponding non-bridged PSs. However, when comparing the absorption maxima of Azo-TPA(+)/TPA(+) and Azo-TPA-Th(+)/TPA-Th(+), there was a 30 nm redshift after the introduction of thiophene. Such changes indicated that the insertion of a  $\pi$ -conjugated unit rather than azo-bridging led to the extension of effective conjugation for D–A type PSs. By referring to the calculated frontier molecular orbitals (FMOs) shown in Fig. S43,† we inferred that the strong D–A interactions in the symmetric side of Azo-TPA-Th(+) played a decisive role in affecting electron delocalization, thereby making the absorption profiles of the azo-bridged PSs resemble those of the corresponding non-bridged ones.

To gain more insight into the mechanism of enhanced photosensitization, we performed theoretical calculations on the two pairs of D–A type PSs, in which both the *trans* and *cis* forms of Azo-TPA-Th(+) and Azo-TPA(+) were calculated. The oscillator strength ( $f$ ), energies of  $S_n$  and  $T_n$  ( $E_{S_n}/E_{T_n}$ ),  $\Delta E_{ST}$ , and  $\xi_{ST}$  are summarized in Tables S1–S6.† According to the calculated  $f$  values, the  $S_1$  of *trans*-Azo-TPA(+) and *cis*-Azo-TPA(+) and the  $S_2$  of *cis*-Azo-TPA-Th(+) were specified as the dark state ( $f = 0$ , 0.05, and 0, respectively). In terms of *trans*-Azo-TPA-Th(+), both  $S_1$  and  $S_2$  were the bright state ( $f = 1.94$  and 1.12, respectively). However, the  $\xi_{ST}$  between  $S_1$  and  $T_n$  ( $n = 1, 2, 3$ ) indicated that

the ISC from  $S_1$  was less likely to occur ( $\xi_{S_1-T_1} = 0.02$  cm\$^{-1}\$,  $\xi_{S_1-T_2} = 0.02$  cm\$^{-1}\$, and  $\xi_{S_1-T_3} = 0$  cm\$^{-1}\$, respectively). In addition, the minimal  $\Delta E_{ST}$  between  $S_1$  and  $T_3$  (0.26 eV) was much larger than that between  $S_2$  and  $T_4$  (0.01 eV) (Fig. 2A). Given the small minimal  $\Delta E_{ST}$  and large  $\xi_{ST}$  ( $\xi_{S_2-T_4} = 0.28$  cm\$^{-1}\$), we inferred that the ISC from  $S_2$  to  $T_4$  was the primary pathway for *trans*-Azo-TPA-Th(+). In contrast, the minimal  $\Delta E_{ST}$  of TPA-Th(+) was calculated to be 0.79 eV between  $S_1$  and  $T_1$ , accompanied by  $\xi_{S_1-T_1}$  of 0.32 cm\$^{-1}\$ (Fig. 2B). Such a comparison suggested that azo-bridging caused a prominent reduction in the minimal  $\Delta E_{ST}$ ,

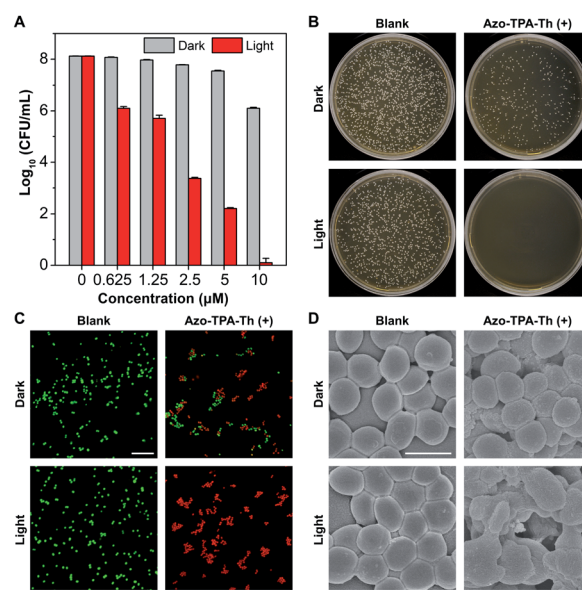


Fig. 3 *In vitro* antibacterial behaviors of Azo-TPA-Th(+) against MRSA. (A) Bacterial viability by the logarithmic number as a function of the concentration of Azo-TPA-Th(+) without and with white light irradiation. (B) Photographs of bacterial colonies formed on agar plates after incubation with Azo-TPA-Th(+) (5  $\mu$ M) without and with white light irradiation. (C) Live/dead staining of bacteria with different treatments, where live and dead bacteria are shown in green and red, respectively. Scale bar: 10  $\mu$ m. (D) SEM images of bacteria with different treatments. Scale bar: 1  $\mu$ m.



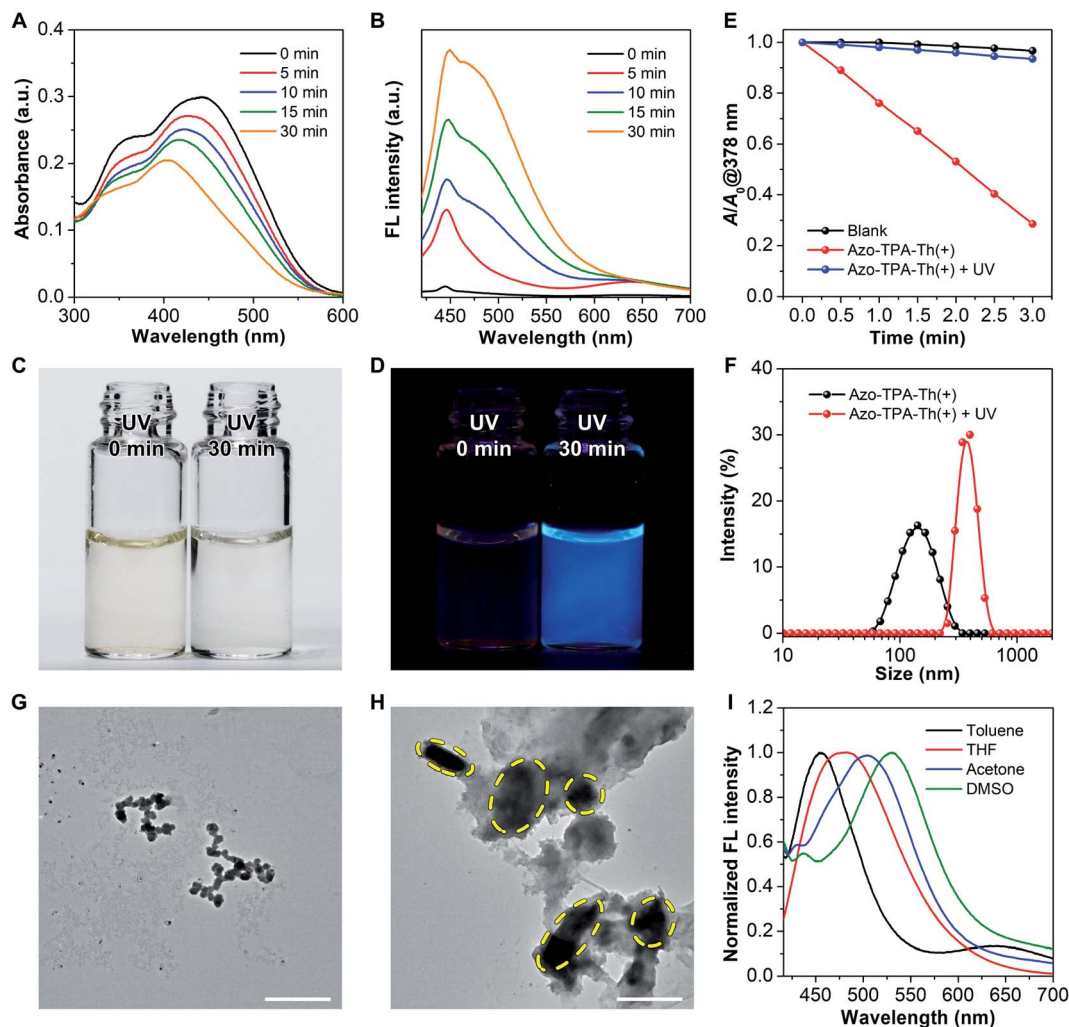
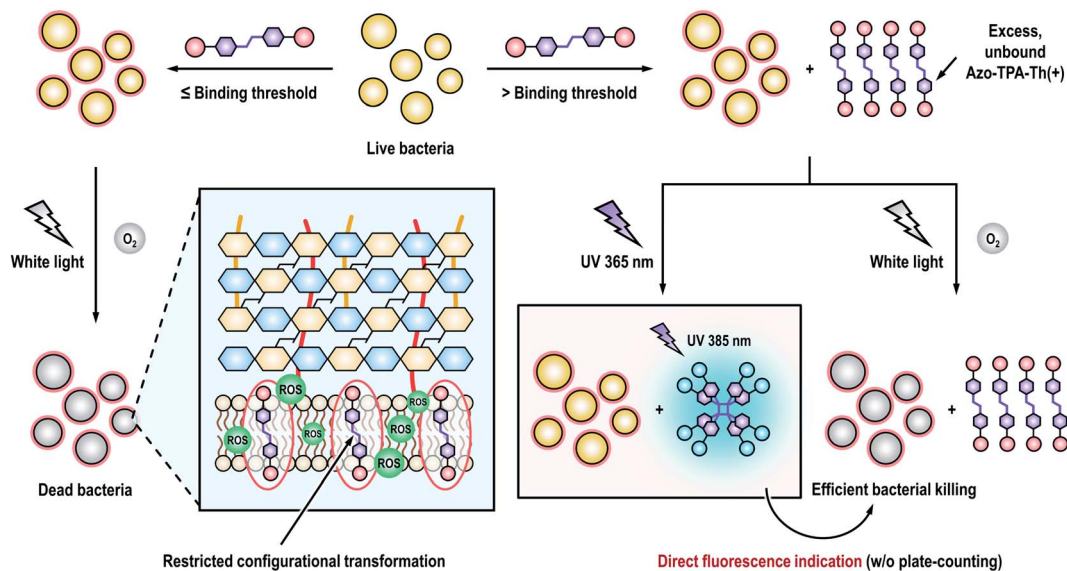


Fig. 4 Responsiveness of Azo-TPA-Th(+) upon 365 nm UV irradiation. (A and B) (A) Absorption and (B) emission spectra of Azo-TPA-Th(+) irradiated for different periods of time. Ex = 385 nm. (C and D) Photographs of Azo-TPA-Th(+) before and after UV irradiation taken under (C) a filament lamp and (D) a 365 nm UV lamp. (E)  $^1\text{O}_2$  measurements before and after UV irradiation. (F) Particle size distribution of Azo-TPA-Th(+) before and after UV irradiation. (G and H) TEM images of Azo-TPA-Th(+) (G) before and (H) after UV irradiation. Scale bars: 500 nm. (I) Normalized emission spectra of Azo-TPA-Th(+) in different organic solvents.

which enabled the increase of  $k_{\text{ISC}}$  and thus efficient ISC. In this case, the excited Azo-TPA-Th(+) in the singlet state easily reached the triplet state *via* ISC, which was followed by type-II and type-I photochemical reactions to generate considerable ROS. Besides, the minimal  $\Delta E_{\text{ST}}$  of *cis*-Azo-TPA-Th(+) was calculated to be 0.58 eV between  $S_1$  and  $T_3$ , with  $\xi_{S_1-T_3}$  of  $0.08 \text{ cm}^{-1}$ . In this case, the ISC process for the *cis* configuration was less likely to occur, which instead favored fluorescence turn-on in the aggregated state (Fig. 2C). Similarly, the minimal  $\Delta E_{\text{ST}}$  of *trans*-Azo-TPA(+), TPA(+), and *cis*-Azo-TPA(+) was determined to be 0.51 eV between  $S_2$  and  $T_4$ , 0.74 eV between  $S_1$  and  $T_1$ , and 0.88 eV between  $S_2$  and  $T_3$ , respectively, together with  $\xi_{S_2-T_4}$  of  $0.17 \text{ cm}^{-1}$ ,  $\xi_{S_1-T_1}$  of  $0.14 \text{ cm}^{-1}$ , and  $\xi_{S_2-T_3}$  of  $0.04 \text{ cm}^{-1}$  (Fig. S44†). These values once again suggested the decreased  $\Delta E_{\text{ST}}$  in azo-bridged *trans*-compounds and increased  $\Delta E_{\text{ST}}$  in azo-bridged *cis*-compounds. To computationally demonstrate the feasibility of type-I photosensitization by all PSs, we

calculated their vertical ionization potentials (VIPs) and vertical electron affinities (VEAs) (Table S7†). As depicted in the equation of  $\text{PS}(T_1) + {}^3\text{O}_2 \rightarrow \text{PS}(T_1)^+ + \text{O}_2^{\cdot-}$ ,  $T_1$  state PSs can sensitize the generation of  $\text{O}_2^{\cdot-}$  by donating an electron to  ${}^3\text{O}_2$ . The prerequisite for this reaction is that the summation of the VIP for the  $T_1$  state ( $\text{VIP}_{T_1}$ ) of PSs and the adiabatic electron affinity (AEA) of  ${}^3\text{O}_2$  ( $\text{AEA}_{\text{O}_2}$ ;  $-3.91 \text{ eV}$  in water) should be negative.<sup>38,39</sup> As shown in Table S7,† the summation of  $\text{VIP}_{T_1}$  and  $\text{AEA}_{\text{O}_2}$  for all PSs was negative, indicating that  $\text{O}_2^{\cdot-}$  could be generated by the photosensitization of all PSs. In terms of type-II photochemical reactions, the  $E_{T_1}$  of all PSs were higher than 0.98 eV which corresponded to the lowest energy required to promote  ${}^3\text{O}_2$  to  ${}^1\text{O}_2$ , indicating that all PSs could sensitize the generation of  ${}^1\text{O}_2$  *via* a direct energy transfer pathway.<sup>40</sup> Taken together, in contrast to unbridged D-A type PSs, azo-bridged *trans*-compounds exhibited decreased  $\Delta E_{\text{ST}}$ , which favored enhanced generation of both type-I and type-II ROS *via* efficient ISC. For





**Scheme 3** Schematic illustration showing the procedure of direct determination of the effective photodynamic bactericidal dose through the appearance of fluorescence.

azo-bridged *cis*-compounds, the  $\Delta E_{ST}$  was increased and the corresponding  $\xi_{ST}$  was decreased. Both changes led to suppressed ISC, which could be employed for the construction of light-responsive fluorescence turn-on systems.

The strong ROS generation capability of Azo-TPA-Th(+) encouraged us to further explore its potential in PDT. As a proof-of-concept demonstration, we studied the application of Azo-TPA-Th(+) in photodynamic killing of drug-resistant bacteria, in which Gram-positive MRSA was selected in view of its responsibility for the largest outbreak of hospital-acquired infection.<sup>41,42</sup> Due to the inherent positive charges, Azo-TPA-Th(+) tended to associate with negatively charged bacteria through electrostatic and/or hydrophobic interactions.<sup>43,44</sup> The quantitative bacterial killing by Azo-TPA-Th(+) was evaluated by plate-counting assay in the absence and presence of white light irradiation. As shown in Fig. 3A, in the absence of white light, there was a moderate concentration-dependent inhibition on bacterial viability, which was attributed to the membrane-damaging effect of cationic species.<sup>45</sup> Upon white light irradiation, the bacterial viability significantly decreased due to the additional destructive effect of the generated ROS. In particular, when the concentration of Azo-TPA-Th(+) reached 10  $\mu$ M, the bacterial killing efficiency was as high as 99.999999%, indicating its outstanding PDT effect. In addition, the corresponding photographs of bacterial colonies formed on agar plates clearly suggested the irradiation-caused enhancement in the inactivation of MRSA (Fig. 3B and S45†). To visualize the antibacterial effect of Azo-TPA-Th(+), we also performed a live/dead fluorescent staining assay. As shown in Fig. 3C, in contrast to the blank group with green fluorescence, the Azo-TPA-Th(+) groups without and with light irradiation showed a pronounced shift in the emission color, in which light irradiation transformed all green-emissive bacteria into red-emissive bacteria, indicating the destructive effect of Azo-TPA-Th(+) on MRSA.

Furthermore, we examined the morphology of MRSA without and with light irradiation by scanning electron microscopy (SEM). As shown in Fig. 3D, the smooth bacterial surface became rough after incubation with Azo-TPA-Th(+) in the absence of light irradiation. In contrast, light irradiation gave rise to obvious bacterial damage with serious membrane splitting and deformation due to the strong photodynamic effect of Azo-TPA-Th(+). These results altogether demonstrated that Azo-TPA-Th(+) was able to photodynamically inactivate drug-resistant bacteria with high killing efficiency.

Since azo-bridging of two molecules of TPA-Th(+) generated an azobenzene structure, the resulting Azo-TPA-Th(+) could respond to UV irradiation by experiencing *trans*-to-*cis* isomerization.<sup>46–48</sup> According to the theoretical calculations, *cis*-Azo-TPA-Th(+) should be potentially efficient in fluorescence emission rather than ROS generation. To verify our hypothesis, we studied the photophysical properties of Azo-TPA-Th(+) in phosphate buffered saline (PBS) before and after UV irradiation. As shown in Fig. 4A, as the irradiation time prolonged, the absorption maximum gradually blue-shifted from 450 to 400 nm, which was accompanied by decreased absorbance. Meanwhile, the emission peak at *ca.* 460 nm started to appear (Fig. 4B). It should be mentioned that the excitation wavelength for Azo-TPA-Th(+) post UV irradiation was fixed at 385 nm as it was the excitation maximum as shown in Fig. S46.† After irradiation for 30 min, the dispersion of Azo-TPA-Th(+) turned from light yellow to near colorless; meanwhile, a pronounced blue emission was observed (Fig. 4C and D). We inferred that the blue-shifted and decreased absorption as well as the fluorescence turn-on phenomenon was attributed to the *trans*-to-*cis* isomerization of Azo-TPA-Th(+),<sup>49</sup> which gave rise to the formation of larger aggregates to activate the AIE phenomenon. Since the absorption peak of TPA-Th(+) largely overlapped with the characteristic absorption of azobenzene, it was difficult to





confirm the configurational transition of Azo-TPA-Th(+) from the UV-vis spectra. However, theoretical calculations indicated that the ROS generation by *cis*-Azo-TPA-Th(+) should be

remarkably decreased when compared to the *trans*-counterpart due to the larger  $\Delta E_{ST}$  and smaller  $\xi_{ST}$ . To exclude the potential interference of *cis*-Azo-TPA-Th(+) on fluorescent ROS indicators,

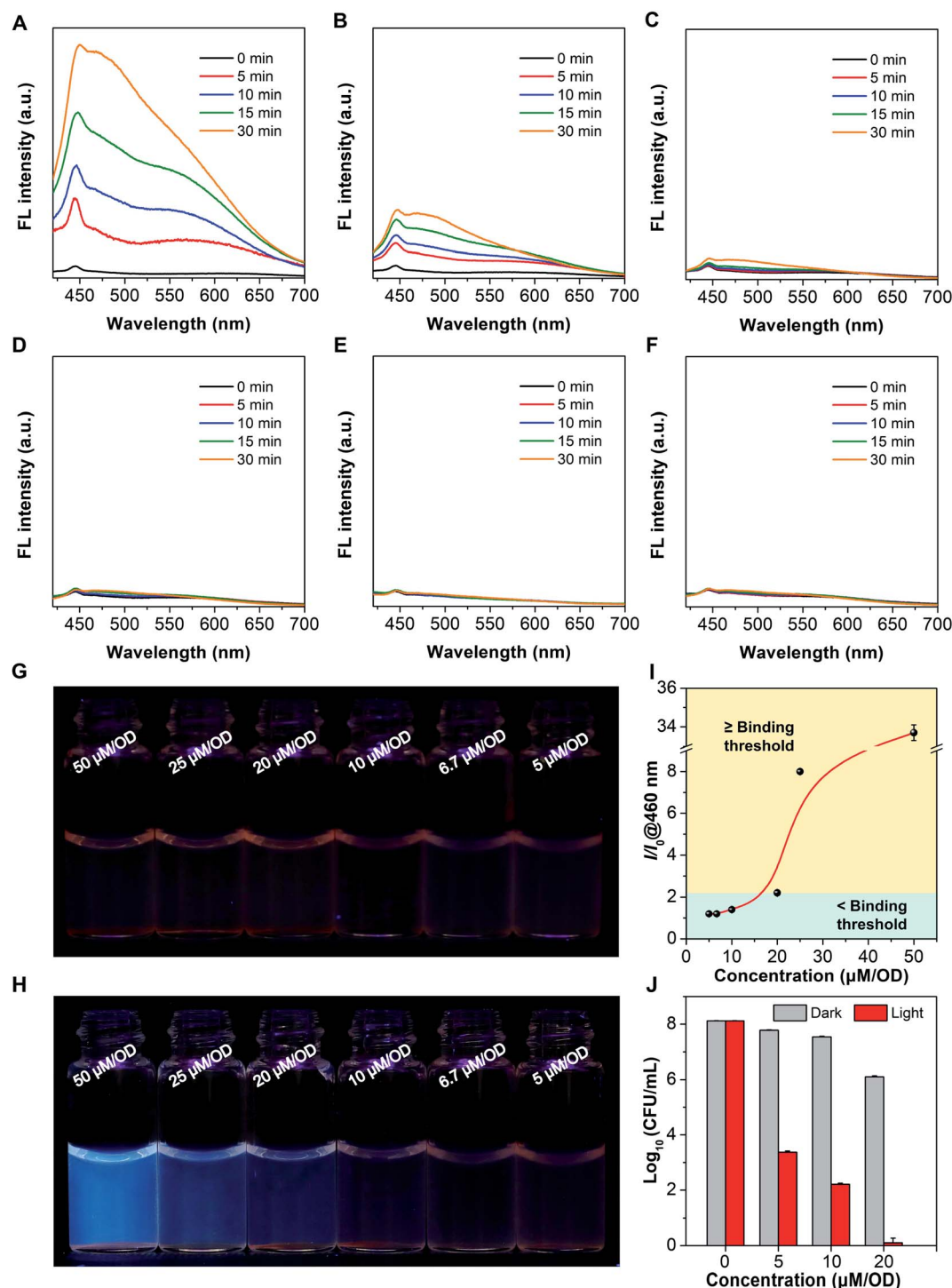


**Fig. 5** Fluorescence determination of the threshold for efficient photodynamic bacterial killing. (A–F) Emission spectra of bacterial suspensions in the presence of Azo-TPA-Th(+) at the relative concentrations of (A) 50  $\mu\text{M}$  per OD, (B) 25  $\mu\text{M}$  per OD, (C) 20  $\mu\text{M}$  per OD, (D) 10  $\mu\text{M}$  per OD, (E) 6.7  $\mu\text{M}$  per OD, and (F) 5  $\mu\text{M}$  per OD irradiated with 365 nm UV light for different periods of time.  $\lambda_{\text{ex}}$  = 385 nm. (G and H) Photographs of bacterial suspensions in the presence of Azo-TPA-Th(+) at different relative concentrations (G) before and (H) after irradiation for 30 min taken under a 365 nm UV lamp. (I) Relative emission intensity ( $I/I_0$ ) of bacterial suspensions in the presence of Azo-TPA-Th(+) at different relative concentrations, in which  $I_0$  and  $I$  represented the emission intensity at 460 nm upon irradiation for 0 min and 30 min, respectively. (J) Bacterial viability by the logarithmic number as a function of the concentration of Azo-TPA-Th(+) without and with white light irradiation.





we performed  $^1\text{O}_2$  measurements before and after UV irradiation with ABDA to indirectly reflect the UV-triggered *trans*-to-*cis* isomerization. As shown in Fig. 4E, upon UV irradiation, ROS generation was remarkably inhibited, with the value of  $A/A_0$  varying from 0.28 to 0.93. In addition, in contrast to the relatively planar *trans*-Azo-TPA-Th(+), the distorted *cis*-configuration was more prone to aggregation in an aqueous environment due to the reduced electrostatic repulsion between pyridinium cations to favor hydrophobic interactions (Fig. S43<sup>†</sup>). As anticipated, UV irradiation caused the hydrodynamic diameter of Azo-TPA-Th(+) to change from *ca.* 140 nm to *ca.* 400 nm (Fig. 4F). Transmission electron microscopy (TEM) characterization further indicated that the small aggregates of Azo-TPA-Th(+) merged into larger aggregates post UV irradiation (Fig. 4G and H). To verify that the aforementioned changes did not result from UV-caused molecular decomposition, we also conducted exactly the same experiment using DMSO as the solvent. As shown in Fig. S47<sup>†</sup>, both the absorption and emission intensities basically remained unchanged, suggesting that the chemical structure of Azo-TPA-Th(+) was not destroyed under experimental conditions. Besides, due to the typical D-A structure, Azo-TPA-Th(+) intrinsically possessed twisted intramolecular charge transfer (TICT) property.<sup>50–52</sup> As shown in Fig. 4I, Azo-TPA-Th(+) exhibited a pronounced solvatochromic phenomenon, with the emission maximum blue-shifting from 533 nm in DMSO to 453 nm in toluene, indicating that Azo-TPA-Th(+) could sense the polarity of its residing environment *via* TICT. The calculated FMOs also suggested the spatial separation of the highest occupied molecular orbital (HOMO) and lowest unoccupied molecular orbital (LUMO) electron clouds, which enabled intramolecular charge transfer from azobenzene and triphenylaniline to pyridinium (Fig. S43<sup>†</sup>). Due to the decreased polarity within the larger aggregates, *cis*-Azo-TPA-Th(+) displayed blue-shifted emission, which accounted for the blue fluorescence of Azo-TPA-Th(+) post UV irradiation.

Motivated by the responsiveness of Azo-TPA-Th(+) to UV light, we postulated that if Azo-TPA-Th(+) is added to bacterial suspensions at a concentration higher than a binding threshold, the excess molecules should undergo photoisomerization upon UV irradiation and thus emit blue fluorescence (Scheme 3). In contrast, if the concentration is lower than a binding threshold, Azo-TPA-Th(+) will associate with the bacteria through electrostatic and/or hydrophobic interactions and locate in the cell membrane. In this case, no evident fluorescence signals should be detected even after UV irradiation due to restricted configurational transformation. As such, we can directly discern whether the concentration of Azo-TPA-Th(+) is sufficiently high for effective bacterial killing based on the appearance of fluorescence post UV irradiation. We first measured the emission spectra of Azo-TPA-Th(+) inoculated by bacteria at different concentrations. The relative concentration, that is, the amount of Azo-TPA-Th(+) per optical density at 600 nm (OD), was employed to indicate different groups. As shown in Fig. 5A–C, when the relative concentrations were set at 50, 25, and 20  $\mu\text{M}$  per OD, respectively, we observed a time-dependent fluorescence turn-on phenomenon post UV irradiation, with the groups at high concentrations exhibiting

remarkable emission enhancement, suggesting the presence of excess Azo-TPA-Th(+). In contrast, when the relative concentrations were fixed at 10, 6.7, and 5  $\mu\text{M}$  per OD, no evident fluorescence turn-on phenomenon was observed, indicating the absence of unbound Azo-TPA-Th(+) for photoisomerization (Fig. 5D–F). Conveniently, such changes could be directly visualized under a 365 nm UV lamp. As shown in Fig. 5G and H, when the relative concentration was  $\geq 20$   $\mu\text{M}$  per OD, the blue fluorescence signals became visible to the naked eye, which was in accordance with the aforementioned result. Furthermore, we plotted a curve to portray the quantitative relationship between emission enhancement and the relative concentration of Azo-TPA-Th(+) (Fig. 5I). According to the results shown in Fig. 5A–H, the binding threshold of Azo-TPA-Th(+) toward MRSA was set at 20  $\mu\text{M}$  per OD, at which the enhancement ratio was calculated to be 2.2-fold. When the relative concentration reached or exceeded the binding threshold, there should exist unbound Azo-TPA-Th(+) to isomerize upon UV irradiation, resulting in the turn-on fluorescence. However, when the relative concentration was less than the binding threshold, Azo-TPA-Th(+) was primarily associated with MRSA with restricted configurational transformation, and, thus, no fluorescence appeared post UV irradiation. Due to the prominent bactericidal capability of Azo-TPA-Th(+), the appearance of fluorescence also implied highly efficient bacterial killing ( $\geq 99.999999\%$ ), as reflected in Fig. 5J. In this case, by conducting a simple fluorescence measurement or simply observing under a 365 nm UV lamp, we could directly discern the effective PDT bactericidal dose within 1 h without performing the time-consuming plate-counting assay, indicating its practicality in real-world applications.

## Conclusions

In summary, we have, for the first time, developed a novel and effective strategy to boost ROS generation by bridging D-A type PSs with the azo group. Theoretical calculations suggested that azo-bridging led to the significant decrease in  $\Delta E_{\text{ST}}$  and thus efficient ISC. Such a strategy not only transformed moderately strong PSs into particularly strong PSs, but also converted particularly weak PSs into moderately strong PSs. In particular, the azo-bridged Azo-TPA-Th(+) exhibited a particularly strong bactericidal effect against clinically relevant MRSA, with the killing efficiency up to 99.999999% upon white light irradiation. Due to the presence of an azobenzene structure, Azo-TPA-Th(+) could undergo *trans*-to-*cis* isomerization upon UV irradiation to form emissive aggregates. By virtue of the fluorescence turn-on property, it was possible to determine the efficient PDT bactericidal dose within 1 h. It should be mentioned that the proof-of-concept azo-bridged PSs are less suited for *in vivo* applications due to their short-wavelength absorption. However, this issue can be addressed by using the well-established approaches to bathochromically shift the absorption spectra of D-A type PSs into the therapeutic window, such as extending the conjugation length and/or enhancing intramolecular D-A interactions.<sup>53–55</sup> This study opens a brand-new avenue for the design of advanced PSs with strong ROS generation and stimu-



responsiveness, holding great potential in high-quality PDT with rapid prediction of the therapeutic outcome.

## Data availability

The data supporting the findings of this study are available within the article and in the ESI.†

## Author contributions

C. Z. and B. H. conceived the project. B. H. carried out the experiments. J. W. performed the theoretical calculations. C. W. participated in the synthesis of chemical compounds. K. X. participated in the live/dead staining experiment. M. X. and S. L. participated in the plate-counting experiment. C. Z. and B. H. wrote the manuscript. All authors discussed the results and contributed to the preparation of the manuscript.

## Conflicts of interest

There are no conflicts to declare.

## Acknowledgements

This work was financially supported by the National Natural Science Foundation of China (52003123 and 92163126) and the Fundamental Research Funds for the Central Universities (Nankai University, 63213121 and 63213058).

## Notes and references

- 1 X. Zhao, J. Liu, J. Fan, H. Chao and X. Peng, *Chem. Soc. Rev.*, 2021, **50**, 4185–4219.
- 2 T. C. Pham, V.-N. Nguyen, Y. Choi, S. Lee and J. Yoon, *Chem. Rev.*, 2021, **121**, 13454–13619.
- 3 Y. Nosaka and A. Y. Nosaka, *Chem. Rev.*, 2017, **117**, 11302–11336.
- 4 P. R. Ogilby, *Chem. Soc. Rev.*, 2010, **39**, 3181–3209.
- 5 Z. Shen, Q. Ma, X. Zhou, G. Zhang, G. Hao, Y. Sun and J. Cao, *NPG Asia Mater.*, 2021, **13**, 39.
- 6 D. Wang, L. Niu, Z.-Y. Qiao, D.-B. Cheng, J. Wang, Y. Zhong, F. Bai, H. Wang and H. Fan, *ACS Nano*, 2018, **12**, 3796–3803.
- 7 A. Turksoy, D. Yildiz and E. U. Akkaya, *Coord. Chem. Rev.*, 2019, **379**, 47–64.
- 8 B. Yuan, H. Wang, J.-F. Xu and X. Zhang, *ACS Appl. Mater. Interfaces*, 2020, **12**, 26982–26990.
- 9 I. Roy, S. Bobbala, R. M. Young, Y. Beldjoudi, M. T. Nguyen, M. M. Cetin, J. A. Cooper, S. Allen, O. Anamimoghdam, E. A. Scott, M. R. Wasielewski and J. F. Stoddart, *J. Am. Chem. Soc.*, 2019, **141**, 12296–12304.
- 10 T. Luo, K. Ni, A. Culbert, G. Lan, Z. Li, X. Jiang, M. Kaufmann and W. Lin, *J. Am. Chem. Soc.*, 2020, **142**, 7334–7339.
- 11 Z. He, S. Tian, Y. Gao, F. Meng and L. Luo, *Front. Chem.*, 2021, **9**, 672917.
- 12 Z. Zhao, H. Zhang, J. W. Y. Lam and B. Z. Tang, *Angew. Chem., Int. Ed.*, 2020, **59**, 9888–9907.
- 13 C. Zhu, R. T. K. Kwok, J. W. Y. Lam and B. Z. Tang, *ACS Appl. Bio Mater.*, 2018, **1**, 1768–1786.
- 14 J. Mei, N. L. C. Leung, R. T. K. Kwok, J. W. Y. Lam and B. Z. Tang, *Chem. Rev.*, 2015, **115**, 11718–11940.
- 15 X. Liu, C. Zhu and B. Z. Tang, *Acc. Chem. Res.*, 2022, **55**, 197–208.
- 16 S. Xu, Y. Duan and B. Liu, *Adv. Mater.*, 2020, **32**, 1903530.
- 17 S. Liu, G. Feng, B. Z. Tang and B. Liu, *Chem. Sci.*, 2021, **12**, 6488–6506.
- 18 W. Zhao, Z. He, Q. Peng, J. W. Y. Lam, H. Ma, Z. Qiu, Y. Chen, Z. Zhao, Z. Shuai, Y. Dong and B. Z. Tang, *Nat. Commun.*, 2018, **9**, 3044.
- 19 Y. Chong, X. Zhang, B. Chen, R. Liu, Z. Wu, G. Zhang, J. Jiang, S. Mukamel and G. Zhang, *J. Phys. Chem. A*, 2021, **125**, 3088–3094.
- 20 L. A. Ortiz-Rodríguez, S. J. Hoehn, A. Loredó, L. Wang, H. Xiao and C. E. Crespo-Hernández, *J. Am. Chem. Soc.*, 2021, **143**, 2676–2681.
- 21 H. Zou, J. Zhang, C. Wu, B. He, Y. Hu, H. H. Y. Sung, R. T. K. Kwok, J. W. Y. Lam, L. Zheng and B. Z. Tang, *ACS Nano*, 2021, **15**, 9176–9185.
- 22 K. M. Farrell, M. M. Brister, M. Pittelkow, T. I. Sølling and C. E. Crespo-Hernández, *J. Am. Chem. Soc.*, 2018, **140**, 11214–11218.
- 23 W. Piao, K. Hanaoka, T. Fujisawa, S. Takeuchi, T. Komatsu, T. Ueno, T. Terai, T. Tahara, T. Nagano and Y. Urano, *J. Am. Chem. Soc.*, 2017, **139**, 13713–13719.
- 24 S. Liu, H. Zhang, Y. Li, J. Liu, L. Du, M. Chen, R. T. K. Kwok, J. W. Y. Lam, D. L. Phillips and B. Z. Tang, *Angew. Chem., Int. Ed.*, 2018, **57**, 15189–15193.
- 25 S. Xu, Y. Yuan, X. Cai, C.-J. Zhang, F. Hu, J. Liang, G. Zhang, D. Zhang and B. Liu, *Chem. Sci.*, 2015, **6**, 5824–5830.
- 26 S. Xu, W. Wu, X. Cai, C.-J. Zhang, Y. Yuan, J. Liang, G. Feng, P. Manghnani and B. Liu, *Chem. Commun.*, 2017, **53**, 8727–8730.
- 27 F. Hu, S. Xu and B. Liu, *Adv. Mater.*, 2018, **30**, 1801350.
- 28 W. Wu, D. Mao, S. Xu, Kenry, F. Hu, X. Li, D. Kong and B. Liu, *Chem*, 2018, **4**, 1937–1951.
- 29 T. Zhou, R. Hu, L. Wang, Y. Qiu, G. Zhang, Q. Deng, H. Zhang, P. Yin, B. Situ, C. Zhan, A. Qin and B. Z. Tang, *Angew. Chem., Int. Ed.*, 2020, **59**, 9952–9956.
- 30 S. Wang, W. Wu, P. Manghnani, S. Xu, Y. Wang, C. C. Goh, L. G. Ng and B. Liu, *ACS Nano*, 2019, **13**, 3095–3105.
- 31 L. Schweighauser, M. A. Strauss, S. Bellotto and H. A. Wegner, *Angew. Chem., Int. Ed.*, 2015, **54**, 13436–13439.
- 32 F. A. Jerca, V. V. Jerca and R. Hoogenboom, *Nat. Rev. Chem.*, 2022, **6**, 51–69.
- 33 L. Dong, Y. Feng, L. Wang and W. Feng, *Chem. Soc. Rev.*, 2018, **47**, 7339–7368.
- 34 H. M. D. Bandara and S. C. Burdette, *Chem. Soc. Rev.*, 2012, **41**, 1809–1825.
- 35 L. Bourré, S. Thibaut, A. Briffaud, N. Rousset, S. Eléouet, Y. Lajat and T. Patrice, *J. Photochem. Photobiol., B*, 2002, **67**, 23–31.
- 36 Z. Liu, H. Zou, Z. Zhao, P. Zhang, G.-G. Shan, R. T. K. Kwok, J. W. Y. Lam, L. Zheng and B. Z. Tang, *ACS Nano*, 2019, **13**, 11283–11293.



- 37 M. Li, T. Xiong, J. Du, R. Tian, M. Xiao, L. Guo, S. Long, J. Fan, W. Sun, K. Shao, X. Song, J. W. Foley and X. Peng, *J. Am. Chem. Soc.*, 2019, **141**, 2695–2702.
- 38 L. Shen, H.-F. Ji and H.-Y. Zhang, *J. Mol. Struct.: THEOCHEM*, 2008, **851**, 220–224.
- 39 J. Llano, J. Raber and L. A. Eriksson, *J. Photochem. Photobiol., A*, 2003, **154**, 235–243.
- 40 K. Wen, H. Tan, Q. Peng, H. Chen, H. Ma, L. Wang, A. Peng, Q. Shi, X. Cai and H. Huang, *Adv. Mater.*, 2022, **34**, 2108146.
- 41 J. Xie, M. Zhou, Y. Qian, Z. Cong, S. Chen, W. Zhang, W. Jiang, C. Dai, N. Shao, Z. Ji, J. Zou, X. Xiao, L. Liu, M. Chen, J. Li and R. Liu, *Nat. Commun.*, 2021, **12**, 5898.
- 42 K. Xue, C. Yang, C. Wang, Y. Liu, J. Liu, L. Shi and C. Zhu, *CCS Chem.*, 2022, **4**, 272.
- 43 X. Liu, M. Xiao, K. Xue, M. Li, D. Liu, Y. Wang, X. Yang, Y. Hu, R. T. K. Kwok, A. Qin, C. Zhu, J. W. Y. Lam and B. Z. Tang, *Angew. Chem., Int. Ed.*, 2021, **60**, 19222–19231.
- 44 M. Kang, C. Zhou, S. Wu, B. Yu, Z. Zhang, N. Song, M. M. S. Lee, W. Xu, F.-J. Xu, D. Wang, L. Wang and B. Z. Tang, *J. Am. Chem. Soc.*, 2019, **141**, 16781–16789.
- 45 Y. Li, F. Liu, J. Zhang, X. Liu, P. Xiao, H. Bai, S. Chen, D. Wang, S. H. P. Sung, R. T. K. Kwok, J. Shen, K. Zhu and B. Z. Tang, *Adv. Sci.*, 2021, **8**, 2001750.
- 46 A. Cembran, F. Bernardi, M. Garavelli, L. Gagliardi and G. Orlandi, *J. Am. Chem. Soc.*, 2004, **126**, 3234–3243.
- 47 S. Mehrparvar, Z. N. Scheller, C. Wölper and G. Haberhauer, *J. Am. Chem. Soc.*, 2021, **143**, 19856–19864.
- 48 H.-B. Cheng, S. Zhang, J. Qi, X.-J. Liang and J. Yoon, *Adv. Mater.*, 2021, **33**, 2007290.
- 49 M. R. Han, Y. Hirayama and M. Hara, *Chem. Mater.*, 2006, **18**, 2784–2786.
- 50 C. Wang, X. Zhao, H. Jiang, J. Wang, W. Zhong, K. Xue and C. Zhu, *Nanoscale*, 2021, **13**, 1195–1205.
- 51 K. Xue, C. Wang, J. Wang, S. Lv, B. Hao, C. Zhu and B. Z. Tang, *J. Am. Chem. Soc.*, 2021, **143**, 14147–14157.
- 52 C. Wang, W. Chi, Q. Qiao, D. Tan, Z. Xu and X. Liu, *Chem. Soc. Rev.*, 2021, **50**, 12656–12678.
- 53 Z. Zhang, W. Xu, M. Kang, H. Wen, H. Guo, P. Zhang, L. Xi, K. Li, L. Wang, D. Wang and B. Z. Tang, *Adv. Mater.*, 2020, **32**, 2003210.
- 54 W. Wu, D. Mao, S. Xu, M. Panahandeh-Fard, Y. Duan, F. Hu, D. Kong and B. Liu, *Adv. Funct. Mater.*, 2019, **29**, 1901791.
- 55 W. Zhu, M. Kang, Q. Wu, Z. Zhang, Y. Wu, C. Li, K. Li, L. Wang, D. Wang and B. Z. Tang, *Adv. Funct. Mater.*, 2021, **31**, 2007026.

